Computational and Applied Mathematics (2026) 45:161
https://doi.org/10.1007/s40314-025-03490-7

Numerical analysis of the Allen–Cahn equation on non-uniform cell sizes

Binhu Xia[1] · Kun Wang[1] · Yunjae Nam[2] · Zhengang Li[2] · Xinpei Wu[3] · Soobin Kwak[3] · Juho Ma[3] · Junseok Kim[3]

Received: 19 August 2025 / Revised: 25 September 2025 / Accepted: 13 October 2025

Abstract

We propose a numerical algorithm for efficiently solving the Allen–Cahn (AC) equation on large computational domains using a non-uniform mesh. The method enhances spatial resolution near interfaces and reduces degrees of freedom in less active regions so that it achieves a balance between accuracy and efficiency. This adaptive mesh strategy enables refined interface tracking without incurring the high cost of globally fine meshes. A fully explicit Euler scheme with a finite difference method (FDM) is used for time discretization, and it provides simplicity and ease of implementation. For spatial discretization on non-uniform grids, special treatment is given to hanging nodes, where grid points do not align with the structured mesh. In such cases, interpolation from neighboring nodes is applied to maintain stability and consistency. The framework can be extended by introducing variable mobility into the AC formulation so that spatially dependent mobility can better capture physical properties and further improve efficiency. Numerical experiments confirm the method's stability and accu-

✉ Junseok Kim
cfdkim@korea.ac.kr

Binhu Xia
20220135@xijing.edu.cn

Kun Wang
2408540402022@stu.xijing.edu.cn

Yunjae Nam
yjnam@korea.ac.kr

Zhengang Li
2024020532@korea.ac.kr

Xinpei Wu
xpwu012@korea.ac.kr

Soobin Kwak
soobin23@korea.ac.kr

Juho Ma
mjh3406@korea.ac.kr

1 School of Science, Xijing University, Xi'an 710049, China

2 Program in Actuarial Science and Financial Engineering, Korea University, Seoul 02841, Republic of Korea

3 Department of Mathematics, Korea University, Seoul 02841, Republic of Korea

Published online: 18 December 2025

racy and show that non-uniform grids significantly enhance computational performance while preserving solution fidelity. These results highlight the suitability of the proposed approach for large-scale simulations of phase-field models, particularly in applications dominated by complex interface dynamics.

Keywords Non-uniform cell sizes · Allen–Cahn equation · Laplace operator

1 Introduction

The phase-field method has been used to model a variety of interfacial phenomena, including topology optimization, crystal growth (Xie et al. 2025), solidification (Xia et al. 2025), and data assimilation (Song et al. 2024a, b; Lu and Wang 2024), due to its ability to capture complex interface dynamics naturally without explicitly tracking interfaces. We consider the Allen–Cahn (AC) equation with a variable mobility defined on a two-dimensional domain $\Omega \subset \mathbb{R}^2$, where spatial adaptivity is introduced through non-uniform cell sizes and the use of variable mobility to improve computational efficiency:

$$\frac{\partial \psi(x,y,t)}{\partial t} = M(x,y)\left[-\frac{F'(\psi(x,y,t))}{\epsilon^2} + \Delta\psi(x,y,t)\right], \quad (x,y) \in \Omega,\ t > 0, \quad (1)$$

where $\psi(x,y,t)$ is an order parameter, ϵ is related to the interface thickness, and $M(x,y)$ is a spatially varying mobility function. The polynomial free energy is defined by $F(\psi) = (\psi^2-1)^2/4$. Figure 1 shows $F(\psi)$ and $F'(\psi)$.

For simplicity, we consider Dirichlet boundary conditions:

$$\psi(x,y,t) = \psi_b, \quad (x,y) \in \partial\Omega,\ t > 0, \quad (2)$$

where $-1 \le \psi_b \le 1$ is a constant. The numerical method is designed to operate on non-uniform meshes that provide higher spatial resolution in critical regions while reducing the overall computational cost. The incorporation of variable mobility further improves the computational efficiency. The AC equation has become a fundamental tool in the study of interface dynamics and phase-field modeling. The AC equation was originally used to model phase separation processes in multi-component systems. Sohaib et al. (2025) showed the efficacy

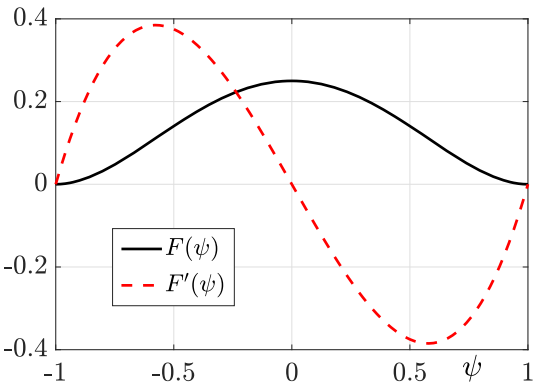

Fig. 1 Polynomial free energy $F(\psi) = (\psi^2-1)^2/4$ (black) and its derivative $F'(\psi)$ (red). The figure shows the double-well potential and the corresponding derivative in phase-field model. (Colour figure online)

of the AC equation in phase separation tasks. Beyond its origins in materials science, where it models grain growth, domain coarsening, and microstructure evolution, the AC equation has found applications in diverse fields such as image processing, computational geometry, fluid dynamics, and biological systems. The following works have shown the wide range of usage of the AC equation. Budd et al. (2021) developed a semi-discrete implicit Euler scheme for the AC equation on graphs and showed its connection to the MBO scheme, and applied it to image segmentation, where their improvements led to more accurate and stable results. Marx-Kuo and Silva (2025) introduced an AC type energy functional on hypersurfaces in closed Riemannian manifolds, established its Γ-convergence to the area functional, analyzed its first and second variations, and related its index and nullity to that of classical AC solutions, applying these results to symmetric solutions on S^1, which denotes the unit circle in two-dimensional plane. Giorgini et al. (2022) analyzed the global well posedness of mass-conserving AC systems coupled with incompressible fluid dynamics. Jornet (2021) modeled biofilm formation using a bistable AC equation incorporating the Allee effect, treated key parameters as random variables, and performed uncertainty quantification via generalized polynomial chaos expansions. Lee and Lee (2025) proposed the anisotropic AC equation with matrix-valued mobility, established its analytical properties such as energy dissipation, maximum principle, and stability, and verified them through numerical experiments.

Various computational methods have been developed to solve phase-field equations with enhanced stability, accuracy, and efficiencyÂ (Hu et al. 2025). These include unconditionally energy-stable schemes for the phase-field equation and binary thermal fluid models on complex or curved geometries (Xia et al. 2024), as well as reduced-order deep learning approaches to accelerate phase-field simulationsÂ (Lv et al. 2025). Adaptive methods are highly effective for solving the AC equation, especially in accurately capturing interface regions and significantly reducing computational cost (Li et al. 2024). Chen et al. (2025) proposed and analyzed adaptive time-stepping schemes to address the divergence issues of standard explicit Euler-type methods for the stochastic AC equation, and they proved strong convergence and demonstrated improved stability and computational efficiency. Bu et al. (2023) proposed adaptive time-stepping techniques within energy-stable SAV-based schemes for the fractional AC equation, and these techniques enhance both efficiency and accuracy in numerical simulations. Guo and Ren (2022) proposed an energy-stable Crank–Nicolson-type method with unequal time steps for the time-fractional AC equation, and it incorporates an adaptive time-stepping algorithm to enhance efficiency while preserving a discrete energy dissipation law. Sun et al. (2021) developed an energy-dissipative adaptive algorithm for the AC equation using a moving mesh strategy combined, which improves numerical performance by concentrating grid points in regions with rapid solution changes, especially in long-time simulations. Zhang et al. (2024) proposed explicit large time-stepping methods for the AC equation using stabilization and Taylor-based exponential approximations. Yang and Kim (2024) presented an energy dissipation-preserving computational method for the phase-field surfactant model, which maintains unconditional stability and accurately captures the long-time dynamics of surfactant-laden phase separation.

The main purpose of this study is to develop an efficient numerical method for solving the AC equation by using a non-uniform mesh that enhances spatial resolution near interfaces while reducing computational cost in less active regions. The proposed approach uses an explicit Euler scheme with FDM and applies interpolation at hanging nodes to ensure numerical stability and consistency. Additionally, the method is improved by incorporating spatially varying mobility to better capture physical properties and enhance computational efficiency.

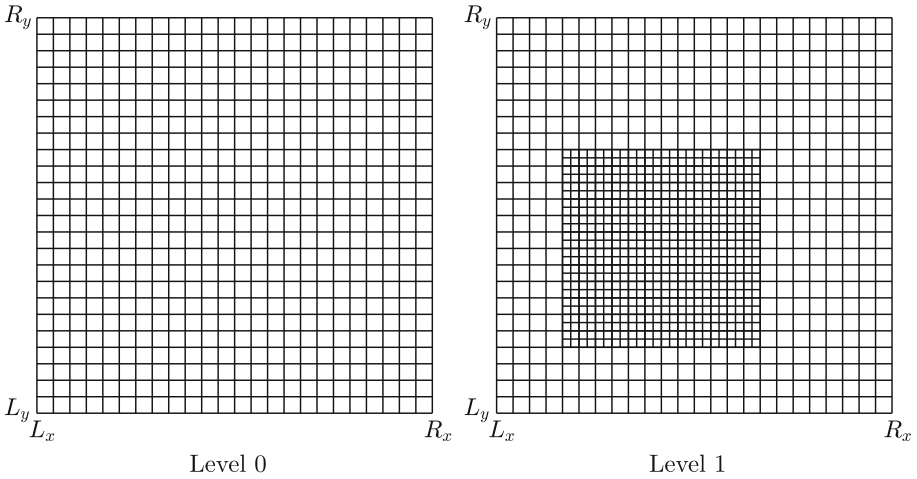

Fig. 2 Schematic of the mesh configuration: The Level 0 grid represents a general uniform mesh, and the Level 1 grid defines the region of interest with a finer mesh

The structure of this article is organized as follows. Section 2 describes the proposed computational method for solving the AC equation using non-uniform grids. Section 3 presents numerical experimental results validating the stability and accuracy of the proposed algorithm. Lastly, Section 4 provides concluding remarks.

2 Computational algorithm

To efficiently solve the AC equation in the two-dimensional domain $\Omega = (L_x, R_x) \times (L_y, R_y)$, we use non-uniform grids. The discrete non-uniform computational domain is defined as $\Omega_h = \{(x_c, y_c) | \, c = 1, \ldots, N_c\}$, where N_c is the number of node points. A common algorithm for generating a non-uniform grid is to use fine grids in the region of interest, while using coarse grids elsewhere as shown in Fig. 2. Although the proposed method is readily extendable to multi-level grids, this study focuses on a two-level grid configuration for clarity of presentation.

Let $\psi_c^n = \psi(x_c, y_c, n\Delta t)$ and $M_c = M(x_c, y_c)$ for $c = 1, \ldots, N_c$, where N_c is the number of node points. The Dirichlet boundary conditions are set as follows: $\psi(L_x, y_c, n\Delta t) = \psi(R_x, y_c, n\Delta t) = \psi(x_c, L_y, n\Delta t) = \psi(x_c, R_y, n\Delta t) = \psi_b$, where we assume ψ_b is a constant for simplicity; it can be space- and time-dependent. We denote the number of time steps N_t and temporal step size Δt. We also denote the neighboring values of ψ_c^n as ψ_l^n, ψ_r^n, ψ_d^n, and ψ_u^n, corresponding to the left, right, down, and up directions, respectively. Then, Eq. (1) is discretized as follows.

$$\frac{\psi_c^{n+1} - \psi_c^n}{\Delta t} = M_c \left(-\frac{F'(\psi_c^n)}{\epsilon^2} + \Delta \psi_c^n \right), \tag{3}$$

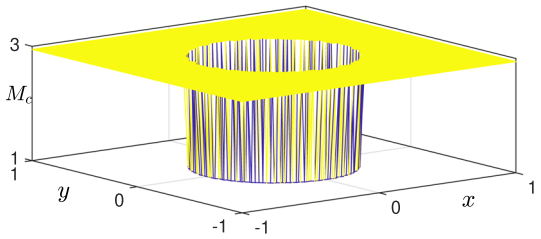

Fig. 3 Schematic of mobility M_c

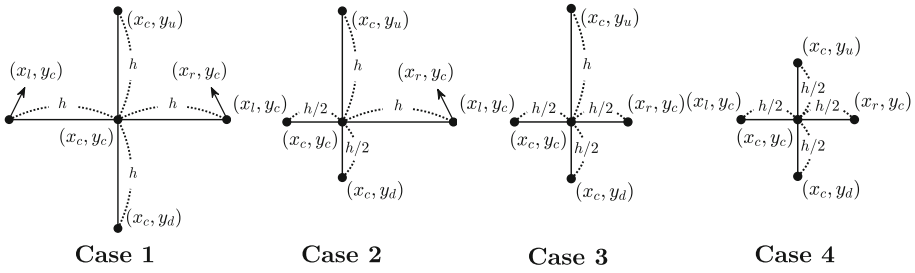

Fig. 4 Schematic of the cases for refined mesh grid

where $\epsilon = mh/(2\sqrt{2}\tanh^{-1}(0.9))$. Here, m is the number of grid points positioned on the interface and h is defined as the maximum mesh size among nodes used in the calculation of the discrete Laplacian operator, for more detailed explanation, see (Kim 2012). We use a time step that satisfies the constraints imposed by the fine grid. However, the constraints on the coarse grid are more relaxed. To create an effect equivalent to enlarging the time step while maintaining stability and thereby achieving a faster evolution on the coarse grid, we define the mobility M_c as follows to compute Eq. (3) on a non-uniform mesh.

$$M_c = \begin{cases} \dfrac{h^2 + 8\varepsilon^2}{h^2 + 2\varepsilon^2}, & \text{if } h_{c,\min} = h, \\ 1, & \text{otherwise,} \end{cases}$$

where $h_{c,\min} = \min\{|x_c - x_l|, |x_c - x_r|, |y_c - y_d|, |y_c - y_u|\}$. Here, otherwise means the case where any one of $|x_c - x_l|, |x_c - x_r|, |y_c - y_d|$, or $|y_c - y_u|$ is $h/2$. A schematic of M_c is displayed in Fig. 3.

To compute $\Delta\psi_c^n$, we consider four cases as shown in Fig. 4. In more detail, **Case 1** and **Case 4** are unique cases as shown in Fig. 4, but **Case 2** and **Case 3** are each further subdivided into four cases due to the necessity of accounting for both directional considerations.

The definition of $\Delta\psi_c^n$ varies by case and is defined as follows:

$$\Delta\psi_c^n = \begin{cases} \dfrac{\psi_l^n + \psi_r^n + \psi_d^n + \psi_u^n - 4\psi_c^n}{h^2}, & |x_c - x_l| = |x_c - x_r| = |y_c - y_d| = |y_c - y_u| = h, \\ \dfrac{4\psi_l^n + 8\psi_r^n + 4\psi_d^n + 8\psi_u^n - 24\psi_c^n}{3h^2}, & |x_c - x_l| = |y_c - y_d| = h, |x_c - x_r| = |y_c - y_u| = \dfrac{h}{2}, \\ \dfrac{4\psi_l^n + 8\psi_r^n + 8\psi_d^n + 4\psi_u^n - 24\psi_c^n}{3h^2}, & |x_c - x_l| = |y_c - y_u| = h, |x_c - x_r| = |y_c - y_d| = \dfrac{h}{2}, \\ \dfrac{8\psi_l^n + 4\psi_r^n + 4\psi_d^n + 8\psi_u^n - 24\psi_c^n}{3h^2}, & |x_c - x_r| = |y_c - y_d| = h, |x_c - x_l| = |y_c - y_u| = \dfrac{h}{2}, \\ \dfrac{8\psi_l^n + 4\psi_r^n + 8\psi_d^n + 4\psi_u^n - 24\psi_c^n}{3h^2}, & |x_c - x_r| = |y_c - y_u| = h, |x_c - x_l| = |y_c - y_d| = \dfrac{h}{2}, \\ \dfrac{4\psi_l^n + 8\psi_r^n + 12\psi_d^n + 12\psi_u^n - 36\psi_c^n}{3h^2}, & |x_c - x_l| = h, |x_c - x_r| = |y_c - y_d| = |y_c - y_u| = \dfrac{h}{2}, \\ \dfrac{8\psi_l^n + 4\psi_r^n + 12\psi_d^n + 12\psi_u^n - 36\psi_c^n}{3h^2}, & |x_c - x_r| = h, |x_c - x_l| = |y_c - y_d| = |y_c - y_u| = \dfrac{h}{2}, \\ \dfrac{12\psi_l^n + 12\psi_r^n + 4\psi_d^n + 8\psi_u^n - 36\psi_c^n}{3h^2}, & |y_c - y_d| = h, |x_c - x_l| = |x_c - x_r| = |y_c - y_u| = \dfrac{h}{2}, \\ \dfrac{12\psi_l^n + 12\psi_r^n + 8\psi_d^n + 4\psi_u^n - 36\psi_c^n}{3h^2}, & |y_c - y_u| = h, |x_c - x_l| = |x_c - x_r| = |y_c - y_d| = \dfrac{h}{2}, \\ \dfrac{4\left(\psi_l^n + \psi_r^n + \psi_d^n + \psi_u^n - 4\psi_c^n\right)}{h^2}, & |x_c - x_l| = |x_c - x_r| = |y_c - y_d| = |y_c - y_u| = \dfrac{h}{2}. \end{cases}$$

We show a simple Level 1 grid in Fig. 5(a). Fig. 5(b) presents specific examples of Cases 1, 2, 3, and 4 on this grid. In **Case 1**, **Case 2**, and **Case 4**, nodes exist in the neighborhood of (x_c, y_c), such as (x_l, y_c), (x_r, y_c), (x_c, y_d), and (x_c, y_u). Therefore, $\Delta\psi_c^n$ is well defined. However, in **Case 3**, no nodes may exist around (x_c, y_c). In this situation, ψ must be defined at a non-existent node, referred to as a hanging node, as shown in Fig. 5(c). If a hanging node exists, the ψ value at that node is computed as the average of the ψ values at the two nodes closest to it.

2.1 Stability analysis

We perform a stability analysis based on the above four cases. For **Case 1** and **Case 4**, the distances between (x_c, y_c) and the four neighboring points are equal, so this situation can be regarded as a uniform grid. According to Ham and Kim (2023), we can derive the time step restriction for **Case 1** as

$$\Delta t = \frac{\epsilon^2 h^2}{\max\{M_c\}(2h^2 + 4\epsilon^2)} = \frac{\epsilon^2 h^2}{2h^2 + 16\epsilon^2}, \tag{4}$$

and the time step restriction for **Case 4** as

$$\Delta t = \frac{\epsilon^2 h^2}{2h^2 + 16\epsilon^2}. \tag{5}$$

Theorem 1 *we consider Case 2. In this case, the mobility $M_c = 1$. Assume that the initial condition satisfies $\|\psi^0\|_\infty \le 1$. Then, for all $n \ge 0$, the numerical solutions of the scheme (3) satisfy $-1 \le \psi^{n+1} \le 1$, for $1 \le i \le N$, if Δt satisfies*

$$\Delta t \le \frac{\epsilon^2 h^2}{2h^2 + 8\epsilon^2}. \tag{6}$$

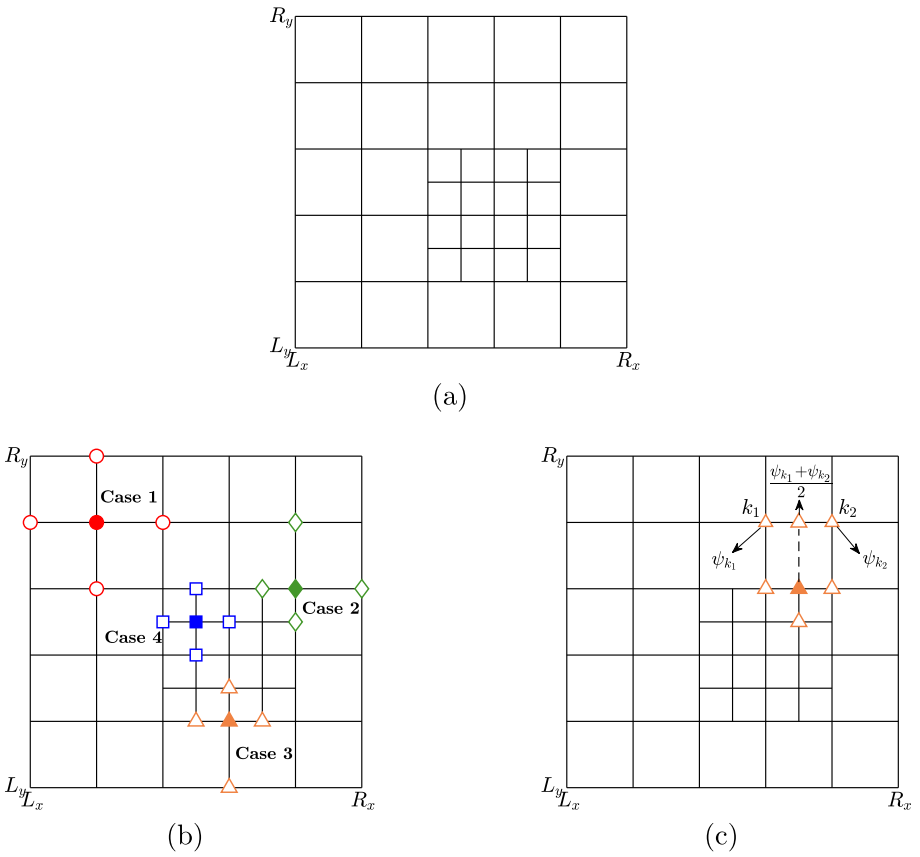

Fig. 5 **(a)** Simple Level 1 grid. **(b)** Examples of Cases 1, 2, 3, and 4 on this grid. **(c)** Hanging node situation in Case 3.

Proof Equation (3) can be rewritten as

$$\psi_c^{n+1} = \psi_c^n + \Delta t \left(\frac{\psi_c^n - (\psi_c^n)^3}{\epsilon^2} + \frac{8\psi_l^n + 4\psi_r^n + 8\psi_d^n + 4\psi_u^n - 24\psi_c^n}{3h^2} \right). \tag{7}$$

The proof is divided into four distinct cases. **I.** $\psi_c^n = 0$ From Eq. (7), we obtain

$$|\Delta t \frac{8\psi_l^n + 4\psi_r^n + 8\psi_d^n + 4\psi_u^n}{3h^2}| \leq 1,$$

and by using the fact that $|\psi^n| \leq 1$, this further reduces to

$$8\frac{\Delta t}{h^2} \leq 1.$$

Therefore,

$$-1 \leq \psi_c^{n+1} \leq 1 \quad \text{if} \quad \Delta t \leq \frac{h^2}{8}. \tag{8}$$

II. $\psi_c^n = 1$ From Eq. (7), we obtain

$$-1 \leq 1 - \Delta t \left(\frac{16}{h^2}\right) \leq 1 + \Delta t \left(\frac{8\psi_l^n + 4\psi_r^n + 8\psi_d^n + 4\psi_u^n - 24}{3h^2}\right) \leq 1. \tag{9}$$

Since $|\psi^n| \leq 1$, there is no condition on the upper bound. We rewrite

$$-1 \leq 1 - \Delta t \left(\frac{16}{h^2}\right), \tag{10}$$

which reduces to

$$\Delta t \leq \frac{h^2}{8}. \tag{11}$$

III. $0 < \psi_c^n < 1$ From Eq. (7), the following upper bounds are derived:

$$\psi_c^n + \Delta t \left(\frac{\psi_c^n(1-\psi_c^n)(1+\psi_c^n)}{\epsilon^2} + 8\frac{1-\psi_c^n}{h^2}\right) \leq 1, \tag{12}$$

$$\Delta t \left(\frac{\psi_c^n(1-\psi_c^n)(1+\psi_c^n)}{\epsilon^2} + 8\frac{1-\psi_c^n}{h^2}\right) \leq 1 - \psi_c^n, \tag{13}$$

$$\Delta t \left(\frac{\psi_c^n(1+\psi_c^n)}{\epsilon^2} + \frac{8}{h^2}\right) \leq 1. \tag{14}$$

We rewrite

$$\Delta t \leq \frac{\epsilon^2 h^2}{2h^2 + 8\epsilon^2} < \frac{\epsilon^2 h^2}{\psi_c^n(1+\psi_c^n)h^2 + 8\epsilon^2}. \tag{15}$$

Since $F'(\psi_c^n) < 0$, the following lower bounds are derived:

$$\psi_c^{n+1} \geq \psi_c^n + \Delta t \left(\frac{8\psi_l^n + 4\psi_r^n + 8\psi_d^n + 4\psi_u^n - 24\psi_c^n}{3h^2}\right), \tag{16}$$

$$\geq \psi_c^n - 8\Delta t \left(\frac{1+\psi_c^n}{h^2}\right) \geq -1. \tag{17}$$

We rewrite

$$1 + \psi_c^n \geq 8\Delta t \left(\frac{1+\psi_c^n}{h^2}\right). \tag{18}$$

By dividing both sides by $1 + \psi_c^n$ and simplifying, we obtain

$$\Delta t \leq \frac{h^2}{8}. \tag{19}$$

Thus, we obtain the condition

$$\Delta t \leq \frac{\epsilon^2 h^2}{2h^2 + 8\epsilon^2}. \tag{20}$$

IV. $-1 \le \psi_c^n < 0$ When $-1 \le \psi_c^n < 0$, it can be equivalently expressed as $0 < -\psi_c^n \le 1$. By multiplying both sides of Eq. (7) by -1, we obtain

$$-\psi_c^{n+1} = -\psi_c^n - \Delta t \left(\frac{\psi_c^n - (\psi_c^n)^3}{\epsilon^2} + \frac{8\psi_l^n + 4\psi_r^n + 8\psi_d^n + 4\psi_u^n - 24\psi_c^n}{3h^2} \right) \tag{21}$$

$$= -\psi_c^n + \Delta t \left(\frac{(-\psi_c^n) - (-\psi_c^n)^3}{\epsilon^2} + \frac{-8\psi_l^n - 4\psi_r^n - 8\psi_d^n - 4\psi_u^n - (-24\psi_c^n)}{3h^2} \right). \tag{22}$$

By examining the right-hand side of Eq. (22) with respect to $-\psi_c^n$, the proofs of **II.** and **III.** are applicable. From the conclusions of **II.** and **III.**, it follows that $\Delta t \le \epsilon^2 h^2/(2h^2 + 8\epsilon^2)$ ensures that $|\psi_c^{n+1}| = |-\psi_c^{n+1}| \le 1$. Since $\epsilon^2 h^2/(2h^2 + 8\epsilon^2) < h^2/8$ for $h > 0$, the proof of the theorem is thereby completed. □

Therefore, we obtain the time step restriction for **Case 2**.

$$\Delta t \le \frac{\epsilon^2 h^2}{2h^2 + 8\epsilon^2}.$$

Theorem 2 *Now we consider Case 3. In this case, the mobility* $M_c = 1$. *Assume that the initial condition satisfies* $\|\psi^0\|_\infty \le 1$. *Consider the fully explicit scheme*

$$\psi_c^{n+1} = \psi_c^n + \Delta t \left(\frac{\psi_c^n - (\psi_c^n)^3}{\epsilon^2} + \Delta_h \psi_c^n \right), \tag{23}$$

where in Case 3 the discrete Laplacian at node c takes the form

$$\Delta_h \psi_c^n = \frac{4\psi_l^n + 8\psi_r^n + 12\psi_d^n + 12\psi_u^n - 36\psi_c^n}{3h^2},$$

where we take this form to represent the other 3 forms since they are equivalent. Then, the numerical solution is bounded by

$$\|\psi^{n+1}\|_\infty \le 1, \qquad n \ge 0, \tag{24}$$

if

$$\Delta t \le \frac{\epsilon^2 h^2}{2h^2 + 12\epsilon^2}. \tag{25}$$

Proof We prove $|\psi_c^{n+1}| \le 1$. We use $|\psi_\alpha^n| \le 1$ for all neighbors $\alpha \in \{l, r, d, u\}$.

I. $\psi_c^n = 0$

Substituting $\psi_c^n = 0$ and the Case 3 Laplacian gives

$$|\psi_c^{n+1}| = \Delta t \left| \frac{4\psi_l^n + 8\psi_r^n + 12\psi_d^n + 12\psi_u^n}{3h^2} \right| \le \Delta t \frac{4 + 8 + 12 + 12}{3h^2} = \Delta t \frac{12}{h^2}. \tag{26}$$

Hence $|\psi_c^{n+1}| \le 1$ if $\Delta t \le h^2/12$.

II. $\psi_c^n = 1$

Here

$$\psi_c^{n+1} = 1 + \Delta t \frac{4\psi_l^n + 8\psi_r^n + 12\psi_d^n + 12\psi_u^n - 36}{3h^2}. \tag{27}$$

Because $\psi_\alpha^n \le 1$, $4\psi_l^n + 8\psi_r^n + 12\psi_d^n + 12\psi_u^n - 36 \le 4+8+12+12-36 = 0$, hence $\psi_c^{n+1} \le 1$. For the lower bound, using $\psi_\alpha^n \ge -1$,

$$\psi_c^{n+1} \ge 1 + \Delta t \frac{4(-1) + 8(-1) + 12(-1) + 12(-1) - 36}{3h^2} = 1 - \Delta t \frac{24}{h^2}. \tag{28}$$

Thus $\psi_c^{n+1} \ge -1$ whenever $1 - 24\Delta t/h^2 \ge -1$, i.e., $\Delta t \le h^2/12$. Therefore, $|\psi_c^{n+1}| \le 1$.

III. $0 < \psi_c^n < 1$

Starting from

$$\psi_c^{n+1} = \psi_c^n + \Delta t \left(\frac{\psi_c^n - (\psi_c^n)^3}{\epsilon^2} + \frac{4(\psi_l^n - \psi_c^n) + 8(\psi_r^n - \psi_c^n) + 12(\psi_d^n - \psi_c^n) + 12(\psi_u^n - \psi_c^n)}{3h^2} \right), \tag{29}$$

we have:

$$\psi_\alpha^n - \psi_c^n \le 1 - \psi_c^n, \tag{30}$$

which yields

$$\Delta_h \psi_c^n \le \frac{4+8+12+12}{3h^2}(1 - \psi_c^n) = \frac{12}{h^2}(1 - \psi_c^n). \tag{31}$$

Hence

$$\psi_c^{n+1} \le \psi_c^n + \Delta t \left(\frac{\psi_c^n - (\psi_c^n)^3}{\epsilon^2} + \frac{12}{h^2}(1 - \psi_c^n) \right). \tag{32}$$

To make sure $\psi_c^{n+1} \le 1$,

$$\Delta t (1 - \psi_c^n) \left(\frac{\psi_c^n (1 + \psi_c^n)}{\epsilon^2} + \frac{12}{h^2} \right) \le 1 - \psi_c^n, \tag{33}$$

and since $1 - \psi_c^n > 0$,

$$\Delta t \le \frac{\epsilon^2 h^2}{h^2 \psi_c^n (1 + \psi_c^n) + 12\epsilon^2}. \tag{34}$$

Since $0 < \psi_i^n (1 + \psi_i^n) < 2$, we obtain the following condition

$$\frac{\epsilon^2 h^2}{2h^2 + 12\epsilon^2} < \frac{\epsilon^2 h^2}{h^2 \psi_c^n (1 + \psi_c^n) + 12\epsilon^2}. \tag{35}$$

Considering the lower bound, since $-1 \le \psi_\alpha^n \le 1$ and $0 < \psi_c^n < 1$, we have

$$\psi_\alpha^n - \psi_c^n \ge -(1 + \psi_c^n), \qquad \Delta_h \psi_c^n \ge -\frac{12}{h^2}(1 + \psi_c^n), \tag{36}$$

and therefore

$$\psi_c^{n+1} \ge \psi_c^n + \Delta t \left(\frac{\psi_c^n - (\psi_c^n)^3}{\epsilon^2} - \frac{12}{h^2}(1 + \psi_c^n) \right). \tag{37}$$

Requiring $\psi_c^{n+1} \ge -1$ gives

$$-1 \le \psi_c^n + \Delta t \left(\frac{(1 + \psi_c^n)\psi_c^n (1 - \psi_c^n)}{\epsilon^2} - \frac{12}{h^2}(1 + \psi_c^n) \right). \tag{38}$$

By dividing both sides by $1+\psi_c^n$, we obtain

$$0 \le 1+\psi_c^n + \Delta t\left(\frac{(1+\psi_c^n)\psi_c^n(1-\psi_c^n)}{\epsilon^2} - \frac{12}{h^2}(1+\psi_c^n)\right), \tag{39}$$

$$0 \le 1+\Delta t\left(\frac{\psi_c^n(1-\psi_c^n)}{\epsilon^2} - \frac{12}{h^2}\right). \tag{40}$$

Since $\psi_c^n(1-\psi_c^n) > 0$, we rewrite

$$0 \le 1-\frac{12\Delta t}{h^2} < 1+\Delta t\left(\frac{\psi_c^n(1-\psi_c^n)}{\epsilon^2} - \frac{12}{h^2}\right), \tag{41}$$

which is guaranteed by $\Delta t \le h^2/12$.

IV. $-1 \le \psi_c^n < 0$ When $-1 \le \psi_c^n < 0$, it can be equivalently expressed as $0 < -\psi_c^n \le 1$. By multiplying both sides of Eq. (23) by -1, we obtain

$$-\psi_c^{n+1} = -\psi_c^n - \Delta t\left(\frac{\psi_c^n-(\psi_c^n)^3}{\epsilon^2} + \frac{4\psi_l^n+8\psi_r^n+12\psi_d^n+12\psi_u^n-36\psi_c^n}{3h^2}\right) \tag{42}$$

$$= -\psi_c^n + \Delta t\left(\frac{(-\psi_c^n)-(-\psi_c^n)^3}{\epsilon^2} + \frac{-4\psi_l^n-8\psi_r^n-12\psi_d^n-12\psi_u^n-(-36\psi_c^n)}{3h^2}\right). \tag{43}$$

By examining the right-hand side of Eq. (43) with respect to $-\psi_c^n$, the proofs of **II.** and **III.** are applicable. From the conclusions of **II.** and **III.**, it follows that $\Delta t \le \epsilon^2h^2/(2h^2+12\epsilon^2)$ ensures that $|\psi_c^{n+1}| = |-\psi_c^{n+1}| \le 1$. Since $\epsilon^2h^2/(2h^2+12\epsilon^2) < h^2/12$ for $h > 0$, the proof of the theorem is thereby completed. □

Therefore, we have the time step restriction for **Case 1**, **Case 2**, **Case 3**, and **Case 4**

$$\Delta t = \frac{\epsilon^2h^2}{2h^2+16\epsilon^2}. \tag{44}$$

3 Numerical tests

Now, we present computational tests to evaluate the performance of the proposed scheme when applied to the AC equation on non-uniform grids. To provide reproducibility of the proposed non-uniform mesh strategy, we describe the refinement procedure in detail. Unless otherwise stated, the computational domain is set to $\Omega = (-1,1)\times(-1,1)$ and discretized with a uniform Level 0 grid of size $N_x = N_y = 64$, corresponding to a mesh step size of $h = 2/(N_x-1)$. A finer Level 1 mesh is then superimposed in the circular region $\sqrt{x^2+y^2} \le 0.5$ as one representative example of a refined area. The refinement ratio between Level 0 and Level 1 is fixed at 2, so that each coarse cell inside the region of interest is subdivided into four finer cells. Consequently, the local mesh width in the refined region becomes $h/2$. The transition between coarse and fine zones follows a two-level rule. This configuration results in a significantly smaller number of nodes than a globally refined 128×128 grid, while it still provides comparable accuracy near the interface.

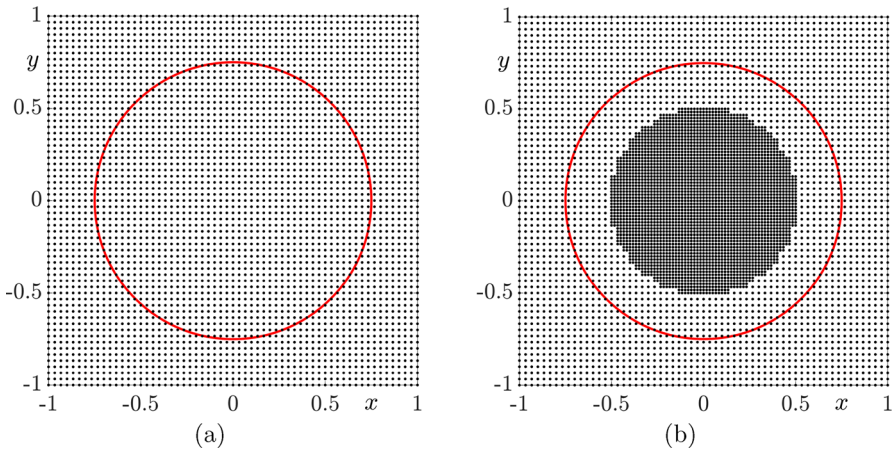

Fig. 6 (a) Uniform grid point at Level 0. (b) Non-uniform grid point at Level 1, with a more finely divided region of interest for numerical experiments. The red line indicates the boundary of the initial condition

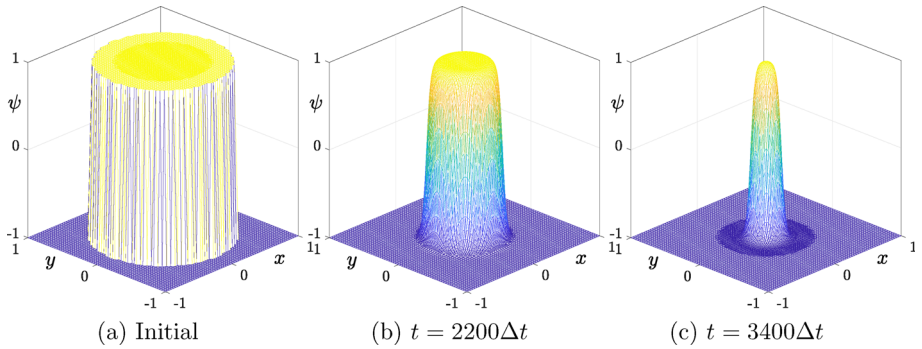

Fig. 7 Temporal evolution of the numerical solutions at (a) $t = 0$, (b) $2200\Delta t$, and (c) $3400\Delta t$

3.1 Mean curvature flow

We investigate mean curvature flow in a two-dimensional domain $\Omega = (-1, 1) \times (-1, 1)$. First, the domain is divided into uniform grids of size $N_x = N_y = 64$, which corresponds to the Level 0 mesh shown in Fig. 6(b). The parameters used in this simulation are $m = 4$, $h = 2/(N_x - 1)$, and $\Delta t = \epsilon^2 h^2/(2h^2 + 16\epsilon^2)$ (Ham and Kim 2023). The initial profile is defined as a circle with radius 0.75 and center at $(0, 0)$.

$$\psi(x, y, 0) = \begin{cases} 1, & \text{if } \sqrt{x^2 + y^2} \le 0.75, \\ -1, & \text{otherwise.} \end{cases} \tag{45}$$

Since our calculation focuses on the region where $\sqrt{x^2 + y^2} \le 0.5$, in the original uniform grid, if $\sqrt{x^2 + y^2} \le 0.5$, we create an additional grid point at the center (see Fig. 6(c)). Then, we perform computations on a non-uniform mesh with a finer grid in the region of interest.

The Dirichlet boundary conditions used in numerical experiments are set as follows: $\psi(-1, y_c, n\Delta t) = \psi(1, y_c, n\Delta t) = \psi(x_c, -1, n\Delta t) = \psi(x_c, 1, n\Delta t) = -1$. The time evolution is illustrated in Fig. 7.

Table 1 CPU time of the numerical experiments under the fine mesh and our proposed non-uniform mesh

	fine mesh	proposed non-uniform mesh
CPU time (seconds)	24.6857	65.5019

In this subsection, we also provide a direct quantitative comparison between the fine mesh (128×128) and our proposed non-uniform mesh. We measure the CPU time of both cases while keeping all other conditions identical, except for the mesh size. We set $\Delta t = \epsilon^2 h^2/(2h^2 + 16\epsilon^2)$ and $M_c = 1$. In Table 1, we can see that applying our proposed non-uniform mesh could significantly reduce the CPU time.

3.2 Random perturbation test

We consider the computational simulation of random perturbation within a two-dimensional domain $\Omega = (-1, 1) \times (-1, 1)$. First, the domain is divided into uniform grids of size $N_x = N_y = 64$. Then, similar to the process in Fig. 6(c), if $\sqrt{x^2 + y^2} \leq 0.5$, we create an additional grid point at the center. In this simulation, the parameters are set as $m = 4$, $h = 2/(N_x - 1)$, and $\Delta t = \epsilon^2 h^2/(2h^2 + 16\epsilon^2)$. The initial condition of the perturbation test is as follows:

$$\psi(x, y, 0) = \text{rand}(x, y), \tag{46}$$

where $\text{rand}(x, y)$ is a random number between -1 and 1. The Dirichlet boundary conditions used in numerical experiments are set as follows: $\psi(-1, y_c, n\Delta t) = \psi(1, y_c, n\Delta t) = \psi(x_c, -1, n\Delta t) = \psi(x_c, 1, n\Delta t) = 0$.

Figure 8 illustrates the time evolution of the phase-field function ψ on a non-uniform grid for the random perturbation test. Figure 8(a) shows the initial condition, where ψ values are randomly distributed between -1 and 1. Over time, the system evolves as shown in Fig. 8(b) and (c), which correspond to $t = 50\Delta t$ and $t = 400\Delta t$, respectively. The initially noisy interface gradually smooths out and forms well-defined phase regions. Figure 8(d) and (e) display the corresponding color maps and mesh structures at $t = 0$ and $t = 400\Delta t$. The non-uniform mesh clearly provides higher resolution in the center, and this enables accurate interface tracking where complexity is high. As time advances, the solution becomes stable, which validates the effectiveness of the proposed numerical algorithm in capturing dynamic interface evolution and maintaining computational efficiency.

3.3 Miro-shaped initial condition

Finally, we examine the Miro-shaped initial condition shown in Fig. 9(a). The parameters match those in Section 3.1, and the non-uniform mesh generation follows the same procedure. The boundary condition is $\psi(-1, y_c, n\Delta t) = \psi(1, y_c, n\Delta t) = \psi(x_c, -1, n\Delta t) = \psi(x_c, 1, n\Delta t) = -1$. The initial pattern forms a rectangular spiral with sharp corners and distinct phase separation, as seen in Fig. 9(a) and (d). The 3D surfaces and color maps confirm that ψ remains strictly within $[-1, 1]$ without overshoot, which shows that the method preserves the maximum principle and maintains stable, well-resolved interfaces. The dynamics are driven by curvature effects characteristic of the AC evolution. Corners relax first because their high curvature induces larger normal velocity, initiating rapid smoothing. By $t = 50\Delta t$,

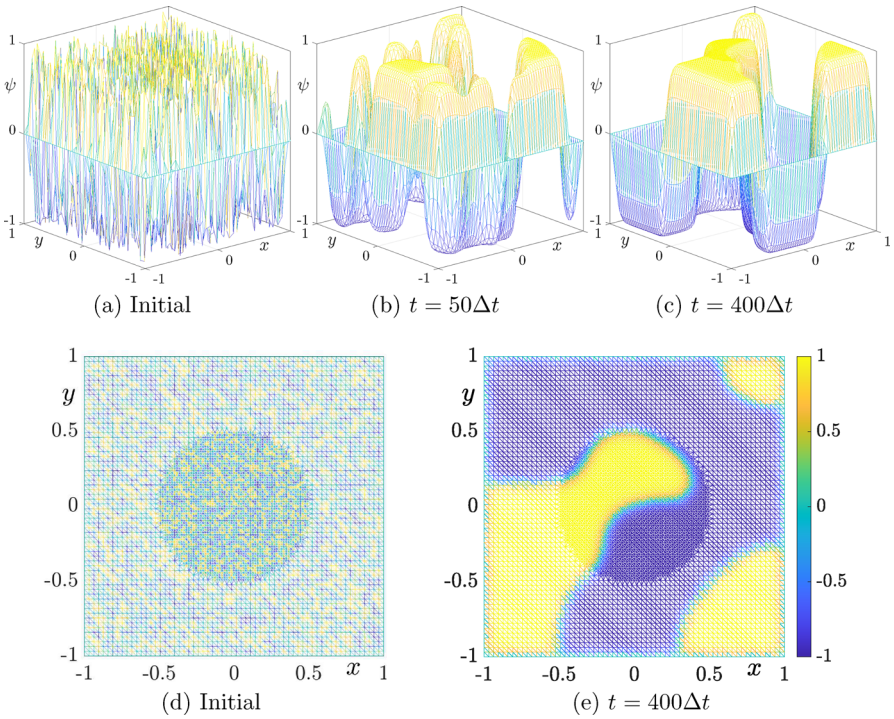

Fig. 8 Numerical solutions at (a) $t = 0$, (b) $50\Delta t$, and (c) $400\Delta t$. Color maps of the computational solutions at (d) initial time and (e) $t = 400\Delta t$

most corners have rounded and the band displays nearly uniform width. At $t = 400\Delta t$, the pattern resembles a smooth spiral with reduced interface length and a smaller region of positive phase. The interface motion follows the sharp-interface law in which the normal velocity is proportional to the negative curvature, so the interface progressively reduces both total curvature and free energy. The imposed Dirichlet boundary fixes the exterior to $\psi = -1$, suppressing boundary artifacts. The spiral remains far from the boundary, so the global constraint does not distort interior dynamics. A slight drift of the spiral center appears in Fig. 9(e), which may arise from minor asymmetry in the initial condition. The non-uniform mesh provides fine resolution near the center of the domain and coarser resolution in the bulk, which achieves multi-resolution with lower computational cost. The Miro test thus confirms that the proposed algorithm resolves complex, highly non-convex interfaces, preserves stability and the maximum principle, and achieves significant efficiency gains on adaptive meshes.

4 Conclusions

In this article, we proposed a computational algorithm for solving the AC equation on non-uniform grids with spatially varying mobility. The method improves computational efficiency by refining the mesh only in regions where detailed interfacial dynamics are significant, while maintaining coarser grids in less active areas. This approach successfully balances the accuracy of interface resolution with the overall computational cost. The discretization strategy

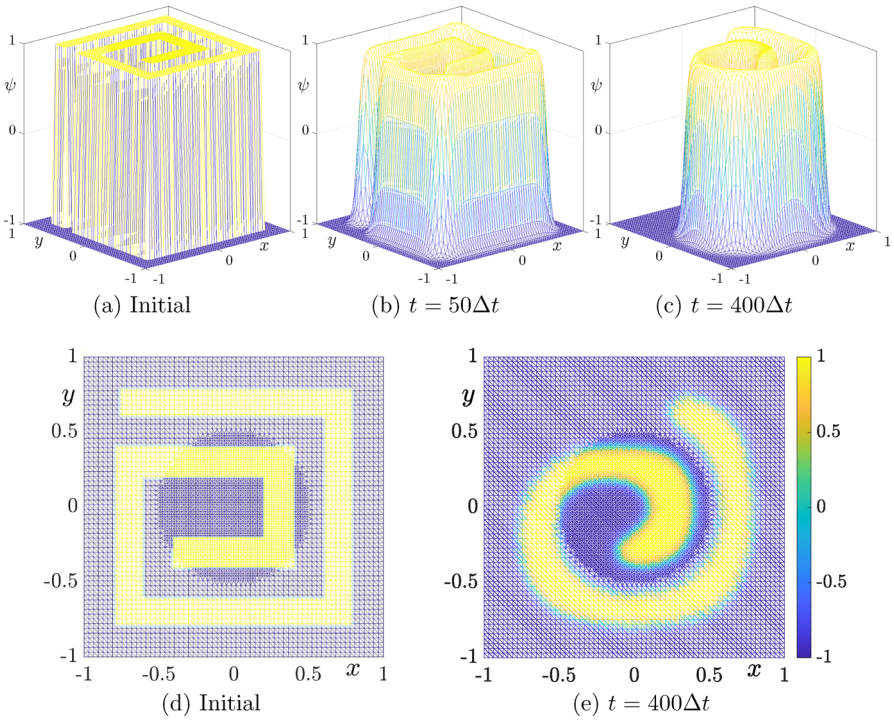

Fig. 9 Numerical solutions at (a) $t = 0$, (b) $50\Delta t$, and (c) $400\Delta t$. Color maps of the numerical solutions at (d) initial time and (e) $t = 400\Delta t$

incorporates an explicit Euler scheme in time and a finite difference scheme adapted to non-uniform grids in space. Special consideration was given to the treatment of hanging nodes to ensure numerical consistency and stability. Through a series of numerical experiments, including mean curvature motion, random perturbation tests, and simulations with complex initial geometries, we demonstrated the robustness of the proposed algorithm. These computational results support the suitability of the proposed approach for large-scale simulations of phase-field models. Future work may involve extending the method to three-dimensional domains or incorporating adaptive time-stepping strategies to further improve performance. An additional advantage of the proposed method lies in its potential applicability to data classification problems. By using local variations in mobility, the algorithm can obtain solutions more efficiently, which is expected to provide strong benefits when applied to classification tasks that require rapid and localized resolution. Nevertheless, some limitations remain. In the current implementation, the values at hanging nodes were determined using linear interpolation, and the adoption of high-order interpolation schemes may further improve the accuracy and stability of the method. Furthermore, although the present scheme imposes constraints on the time step size due to the explicit time discretization, the extension of the scheme to unconditionally stable methods is an important direction for future research. Possible candidates include semi-implicit approaches such as the Saul'yev scheme.

Acknowledgements The corresponding author (J.S. Kim) was supported by the National Research Foundation of Korea(NRF) grant funded by the Korea government(MSIT) (No. 2022R1A2C1003844). The authors express their gratitude to the reviewers for their valuable and insightful comments that greatly assisted the revision of this article.

Author Contributions Conceptualization: Binhu Xia, Junseok Kim; Data curation: Zhengang Li, Xinpei Wu, Juho Ma; Formal analysis: Yunjae Nam, Kun Wang, Zhengang Li, Soobin Kwak; Investigation: Yunjae Nam, Kun Wang, Zhengang Li; Methodology: Binhu Xia, Yunjae Nam, Soobin Kwak, Junseok Kim; Project administration: Junseok Kim; Supervision: Junseok Kim; Validation: Binhu Xia, Soobin Kwak, Junseok Kim; Visualization: Yunjae Nam, Zhengang Li, Xinpei Wu, Juho Ma; Writing–original draft preparation: Binhu Xia, Yunjae Nam, Zhengang Li, Xinpei Wu, Soobin Kwak, Juho Ma; Writing–review & editing: Zhengang Li, Xinpei Wu, Soobin Kwak, Juho Ma, Junseok Kim;

Declarations

Conflict of interest The authors declare there are no conflicts of interest.

Use of AI tools declaration The authors declare they have not used Artificial Intelligence (AI) tools in the creation of this article.

References

Bu L, Wu J, Mei L, Wang Y (2023) Second-order linear adaptive time-stepping schemes for the fractional Allen-Cahn equation. Comput. Math Appl 145:260–274. https://doi.org/10.1016/j.camwa.2023.06.027

Budd J, van Gennip Y, Latz J (2021) Classification and image processing with a semi-discrete scheme for fidelity forced Allen–Cahn on graphs *GAMM Mitteilungen* 44(1), e202100004. https://doi.org/10.1002/gamm.202100004

Chen C, Dang T, Hong J (2025) Strong convergence of adaptive time-stepping schemes for the stochastic Allen-Cahn equation. IMA. J Numer Anal 45(1):404–450. https://doi.org/10.1093/imanum/drae009

Giorgini A, Grasselli M, Wu H (2022) On the mass-conserving Allen–Cahn approximation for incompressible binary fluids *J. Funct. Anal.* 283(9), 109631. https://doi.org/10.1016/j.jfa.2022.109631

Guo S, Ren J (2022) A novel adaptive Crank-Nicolson-type scheme for the time fractional Allen-Cahn model. Appl Math Lett 129:107943. https://doi.org/10.1016/j.aml.2022.107943

Ham S, Kim J (2023) Stability analysis for a maximum principle preserving explicit scheme of the Allen-Cahn equation. Math Comput Simul 207:453–465. https://doi.org/10.1016/j.matcom.2023.01.016

Hu X, Xia Q, Xia B, Li Y (2025) A second-order accurate numerical method with unconditional energy stability for the Lifshitz-Petrich equation on curved surfaces. Appl Math Lett 163:109439. https://doi.org/10.1016/j.aml.2024.109439

Jornet M (2021) Modeling of Allee effect in biofilm formation via the stochastic bistable Allen-Cahn partial differential equation. Stoch. Anal Appl 39(1):22–32. https://doi.org/10.1080/07362994.2020.1777163

Kim J (2012) Phase-field models for multi-component fluid flows. Commun. Comput Phys 12(3):613–661. https://doi.org/10.4208/cicp.301110.040811a

Lee G, Lee S (2025) Allen-Cahn equation with matrix-valued anisotropic mobility in two-dimensional space. Comput. Appl Math 44(3):122. https://doi.org/10.1007/s40314-024-03079-6

Li R, Gao Y, Chen Z (2024) Adaptive discontinuous Galerkin finite element methods for the Allen-Cahn equation on polygonal meshes. Numer. Algorithms 95(4):1981–2014. https://doi.org/10.1007/s11075-023-01635-5

Lu Z, Wang J (2024) A novel and efficient multi-scale feature extraction method for EEG classification *AIMS Math.* 9(6), 16605–16622. https://doi.org/10.3934/math.2024805

Lv Z, Song X, Feng J, Xia Q, Xia B, Li Y (2025) Reduced-order prediction model for the Cahn–Hilliard equation based on deep learning *Eng. Anal. Bound. Elem.* 172, 106118. https://doi.org/10.1016/j.enganabound.2025.106118

Marx-Kuo J, Silva ÉM (2025) Geometric variations of an Allen-Cahn energy on hypersurfaces. Calc Var Partial Differ Equ 64:1–58. https://doi.org/10.1007/s00526-025-03016-3

Song X, Xia Q, Kim J, Li Y (2024) An unconditional energy stable data assimilation scheme for Navier-Stokes-Cahn-Hilliard equations with local discretized observed data. Comput. Math Appl 164:21–33. https://doi.org/10.1016/j.camwa.2024.03.018

Song X, Xia B, Li Y (2024) An efficient data assimilation based unconditionally stable scheme for Cahn-Hilliard equation. Comput. Appl Math 43(3):121. https://doi.org/10.1007/s40314-024-02632-7

Sohaib M, Shah A, Furati KM (2025) Khaliq H, A numerical scheme for time-fractional Allen-Cahn equation with application in phase separation, Int. J Comput Math 102(3):449–464. https://doi.org/10.1080/00207160.2024.2420681

Sun JW, Qian X, Zhang H, Song SH (2021) Novel energy dissipative method on the adaptive spatial discretization for the Allen-Cahn equation. Chin Phys B 30(7):070201. https://doi.org/10.1088/1674-1056/abe37b

Xia B, Xi X, Yu R, Zhang P (2024) Unconditional energy-stable method for the Swift-Hohenberg equation over arbitrarily curved surfaces with second-order accuracy. Appl Numer Math 198:192–201. https://doi.org/10.1016/j.apnum.2024.01.005

Xia Q, Lai S, Kim J, Li Y (2025) Phase field modeling of melting and solidification dynamics in metallic powders during the bed fusion process. Commun. Nonlinear Sci Numer Simul 146:108762. https://doi.org/10.1016/j.cnsns.2025.108762

Xie W, Wang Z, Kim J, Sun X, Li Y (2025) A novel ensemble Kalman filter based data assimilation method with an adaptive strategy for dendritic crystal growth *J. Comput. Phys.* 524, 113711. https://doi.org/10.1016/j.jcp.2024.113711

Yang J, Kim J (2024) An adapted energy dissipation law-preserving numerical algorithm for a phase-field surfactant model. Comput. Appl Math 43(1):31. https://doi.org/10.1007/s40314-023-02537-x

Zhang H, Qian X, Song S (2024) Third-order accurate, large time-stepping and maximum-principle-preserving schemes for the Allen-Cahn equation. Numer. Algorithms 95(3):1213–1250. https://doi.org/10.1007/s11075-023-01606-w